

This is a repository copy of *Lifetimes of excited states in  $\{^1S\}^{\{16\}}\{^1S\}C$  as a benchmark for ab initio developments.*

White Rose Research Online URL for this paper:

<https://eprints.whiterose.ac.uk/217211/>

Version: Published Version

---

**Article:**

Petri, Marina [orcid.org/0000-0002-3740-6106](https://orcid.org/0000-0002-3740-6106) and Paschalis, Stefanos [orcid.org/0000-0002-9113-3778](https://orcid.org/0000-0002-9113-3778) (2024) Lifetimes of excited states in  $\{^1S\}^{\{16\}}\{^1S\}C$  as a benchmark for ab initio developments. *European Physical Journal A : Hadrons and Nuclei*. 181. ISSN 1434-601X

<https://doi.org/10.1140/epja/s10050-024-01396-2>

---

**Reuse**

This article is distributed under the terms of the Creative Commons Attribution (CC BY) licence. This licence allows you to distribute, remix, tweak, and build upon the work, even commercially, as long as you credit the authors for the original work. More information and the full terms of the licence here:

<https://creativecommons.org/licenses/>

**Takedown**

If you consider content in White Rose Research Online to be in breach of UK law, please notify us by emailing [eprints@whiterose.ac.uk](mailto:eprints@whiterose.ac.uk) including the URL of the record and the reason for the withdrawal request.



# Lifetimes of excited states in $^{16}\text{C}$ as a benchmark for ab initio developments

M. Mathy<sup>1</sup>, M. Petri<sup>2,a</sup>, R. Roth<sup>1</sup>, L. Wagner<sup>1</sup>, S. Heil<sup>1</sup>, A. D. Ayangeakaa<sup>3,10,11</sup>, S. Bottoni<sup>3,12</sup>, M. P. Carpenter<sup>3</sup>, H. L. Crawford<sup>4</sup>, P. Fallon<sup>4</sup>, J. Elson<sup>5</sup>, J. Kinnison<sup>5</sup>, T. Lauritsen<sup>3</sup>, I.-Y. Lee<sup>4</sup>, A. O. Macchiavelli<sup>6</sup>, S. Paschalis<sup>2</sup>, W. Reviol<sup>3</sup>, D. G. Sarantites<sup>5</sup>, I. Syndikus<sup>1</sup>, S. L. Tabor<sup>7</sup>, M. Wiedeking<sup>4,8,9</sup>, S. Zhu<sup>3,†</sup>

- <sup>1</sup> Institut für Kernphysik, Technische Universität Darmstadt, Darmstadt, Germany  
<sup>2</sup> School of Physics, Engineering and Technology, University of York, Heslington, York, UK  
<sup>3</sup> Physics Division, Argonne National Laboratory, Argonne, IL, USA  
<sup>4</sup> Nuclear Science Division, Lawrence Berkeley National Laboratory, Berkeley, CA, USA  
<sup>5</sup> Chemistry Department, Washington University, St. Louis, MO, USA  
<sup>6</sup> Physics Division, Oak Ridge National Laboratory, Oak Ridge, TN, USA  
<sup>7</sup> Department of Physics, Florida State University, Tallahassee, FL, USA  
<sup>8</sup> SSC Laboratory, iThemba LABS, PO Box 722, Somerset West, South Africa  
<sup>9</sup> School of Physics, University of the Witwatersrand, Johannesburg, South Africa  
<sup>10</sup> Present address: Department of Physics and Astronomy, University of North Carolina at Chapel Hill, Chapel Hill, NC 27599, USA  
<sup>11</sup> Triangle Universities Nuclear Laboratory, Duke University, Durham, NC 27708, USA  
<sup>12</sup> Present address: Dipartimento di Fisica, Università degli Studi di Milano and INFN Sez. Milano, Milano, Italy

Received: 23 November 2023 / Accepted: 12 August 2024

© The Author(s) 2024

Communicated by Wolfram Korten

**Abstract** Lifetimes of higher-lying states ( $2_2^+$  and  $4_1^+$ ) in  $^{16}\text{C}$  have been measured, employing the Gammasphere and Microball detector arrays, as key observables to test and refine ab initio calculations based on interactions developed within chiral Effective Field Theory. The presented experimental constraints to these lifetimes of  $\tau(2_2^+) = [244, 446]$  fs and  $\tau(4_1^+) = [1.8, 4]$  ps, combined with previous results on the lifetime of the  $2_1^+$  state of  $^{16}\text{C}$ , provide a rather complete set of key observables to benchmark the theoretical developments. We present No-Core Shell-Model calculations using state-of-the-art chiral 2- (NN) and 3-nucleon (3N) interactions at next-to-next-to-next-to-leading order for both the NN and the 3N contributions and a generalized natural-orbital basis (instead of the conventional harmonic-oscillator single-particle basis) which reproduce, for the first time, the experimental findings remarkably well. The level of agreement of the new calculations as compared to the CD-Bonn meson-exchange NN interaction is notable and presents a critical benchmark for theory.

## 1 Introduction

Ab initio nuclear structure theories using 2- (NN) plus 3-nucleon (3N) Hamiltonians derived from chiral effective field theory (EFT) (see [1] for a recent review) connect to the underlying physics of the strong interaction and provide a unique opportunity to understand the nuclear structure and its evolution from first principles. Although recent calculations of excitation energies with chiral NN+3N interactions in light and medium-mass (mainly closed-shell) nuclei have been successful, their extension to other observables remains a challenge. Therefore, data on electromagnetic properties provide an exciting opportunity to constrain NN+3N Hamiltonians derived from chiral EFT in ab initio calculations ranging from Nuclear Lattice EFT [2] to the No-Core Shell Model (NCSM) [3,4]. The strong sensitivity to the underlying interaction makes these observables prime candidates for testing next-generation chiral Hamiltonians, e.g., the consistent chiral NN+3N interactions at next-to-next-to-next-to-leading order that are being developed now. At the same time, they are a critical test for new ab initio approaches, e.g., the nuclear lattice EFT and shell model with valence-space interactions from an in-medium similarity renormalization group evolution, which are presently being extended to the description of transition observables.

<sup>†</sup> Deceased: S. Zhu.

<sup>a</sup> e-mail: [marina.petri@york.ac.uk](mailto:marina.petri@york.ac.uk) (corresponding author)

Large-scale NCSM calculations, starting from realistic Hamiltonians without adjustable parameters or effective charges, have been performed for low-lying states of even-even carbon isotopes with  $A = 10 - 20$  [5] in order to understand their structural evolution with increasing neutron number. Overall, a strong sensitivity of the electromagnetic observables in  $^{16}\text{C}$  to the details of the nuclear Hamiltonian has been found. In particular, a strong suppression of the  $2_2^+ \rightarrow 0_{g.s.}^+$  transition has been predicted when the 3N interaction is included. The sensitivity to the presence of the 3N interaction is remarkable. The  $2_2^+ \rightarrow 0_{g.s.}^+$  transition strength is suppressed by a factor of  $\approx 7$  in the calculation with the chiral 3N compared to chiral NN only. At the same time the CD-Bonn potential, a well-tested NN interaction constructed within meson exchange theory and very successful in the description of  $p$ -shell spectroscopy, predicts a transition strength larger by a factor of  $\approx 20$  than the chiral NN+3N interaction. An experimental study of  $^{16}\text{C}$  [6] points to the inclusion of 3N forces in order to reproduce the experimental branching ratios of the  $2_2^+ \rightarrow 2_1^+$  and  $2_2^+ \rightarrow 0_{g.s.}^+$  transitions that have been constrained to  $>91.2\%$  and  $<8.8\%$ , respectively.

The lifetimes of the higher-lying states in  $^{16}\text{C}$  are key observables to understand the role of 3N forces and to benchmark ab initio calculations employing interactions developed within chiral effective field theory; see Fig. 1 for the current experimental information on the low-lying levels of  $^{16}\text{C}$ . A recent experimental investigation of the lifetime of the  $2_2^+$  state [7] was inconclusive, delivering only a lower limit for the lifetime with a strong dependency on the energy of the  $\gamma$ -ray transition. In this work, we present an improved measurement of the lifetime of the  $2_2^+$  state and a lower limit for the lifetime of the  $4_1^+$  state in  $^{16}\text{C}$ . We combine our results with previous results on the lifetime of the  $2_1^+$  state [6,8] and we compare those with new ab initio calculations. Our work provides a rather complete set of key observables to

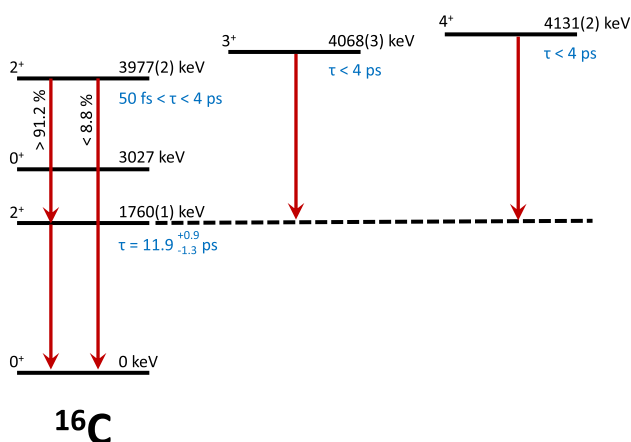


**Fig. 1** Spectroscopic information on the bound excited states of  $^{16}\text{C}$ ; lifetime information are extracted from Refs. [6–9]

benchmark present and future ab initio calculations. Indeed, new NCSM calculations using state-of-the-art chiral NN+3N interactions at next-to-next-to-next-to-leading order for both the NN and the 3N contributions reproduce the experimental findings remarkably well.

## 2 Experimental details, analysis and results

To measure lifetimes of higher-lying excited states in  $^{16}\text{C}$ , a Doppler-Shift Attenuation Method (DSAM) experiment was employed at the Tandem Linac Accelerator System (ATLAS) of the Argonne National Laboratory (ANL). A 40 MeV  $^9\text{Be}$  beam bombarded a 1.38 mg/cm $^2$   $^9\text{Be}$  target. To realise the Doppler-Shift Attenuation measurement, a 38.4 mg/cm $^2$  Au degrader was evaporated on the back of the  $^9\text{Be}$  target. Excited states in  $^{16}\text{C}$  were accessed through the fusion-evaporation channel  $^9\text{Be}(^9\text{Be}, 2p)^{16}\text{C}$ , as demonstrated in [8]. The emitted  $\gamma$  rays were measured using the Gammasphere array [10], consisting of 87 Compton suppressed HPGe detectors positioned at 16 different polar angles,  $\theta$ , with respect to the beam axis. To select events that correspond to  $^{16}\text{C}$  (i.e., the two-proton (2p) exit channel of the fusion-evaporation reaction), the Microball charged-particle detector [11] was placed inside the scattering chamber and operated in coincidence with Gammasphere.

A two-dimensional (2D) plot of the laboratory energy of the emitted  $\gamma$  rays (i.e., not Doppler corrected) versus the Gammasphere detector angle  $\theta$  in coincidence with two protons detected in Microball are shown in Fig. 2. The  $2_1^+$  and  $4_1^+$  decays of  $^{16}\text{C}$  are clearly seen as vertical lines, which indicates that the decay occurs after the nucleus has stopped in the Au degrader (decaying thus with zero velocity ( $\beta = v/c = 0$ ) and not presenting any Doppler shift). This puts a lower limit for the lifetime of the  $4_1^+$  state, discussed in Sect. 2.2. The  $3_1^+ \rightarrow 2_1^+$  transition of  $^{16}\text{C}$  overlaps with the  $7/2_1^+ \rightarrow 5/2_1^+$  state of  $^{15}\text{N}$  (the relatively strong 1p2n exit channel); the latter channel produces random background in Microball which could not be removed in the present analysis and which hinders any conclusion on the lifetime of the  $3_1^+$  state. The  $^{22}\text{Ne}$  lines originate from ( $^9\text{Be}, 2pn$ ) reactions induced by oxygen layers on the surface of the target. This contamination in the  $\gamma$ -ray spectrum has been used to validate the analysis procedure with the help of the known lifetime of the  $4^+$  state of  $^{22}\text{Ne}$ , see Fig. 3; more details can be found in [12]. This also demonstrates the sensitivity of our setup to lifetimes of the order of few hundred femtoseconds. The  $2_2^+$  state of  $^{16}\text{C}$  cannot be seen in the 2p gated spectrum because it is weakly populated in the fusion-evaporation reaction and the  $\gamma$ -ray energy spectrum is dominated by background. More detailed investigations have thus been performed, as described in the Sect. 2.1.

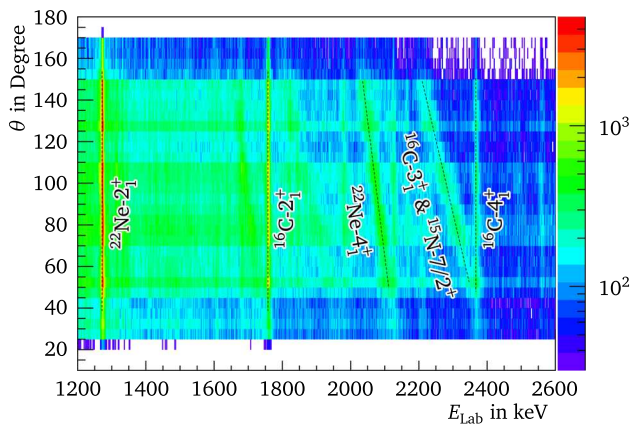


**Fig. 2** Radiation-detection angle  $\theta$  versus laboratory energy  $E_{\text{Lab}}$  for 2p Microball-gated  $\gamma$ -ray events for the target/degrader setting. Dominant  $\gamma$  rays from other fusion-evaporation reactions, as well as those from the reaction channel of interest are indicated with a dotted line, the corresponding isotope and the initial state of the  $\gamma$ -ray transition is given. Other transitions visible but not marked on the plot correspond to the  $^{23}\text{Ne } 7/2^+ \rightarrow 5/2^+$  1701 keV transition and to the  $^{15}\text{N } 5/2_2^+ \rightarrow 5/2_1^+$  1884 keV transition

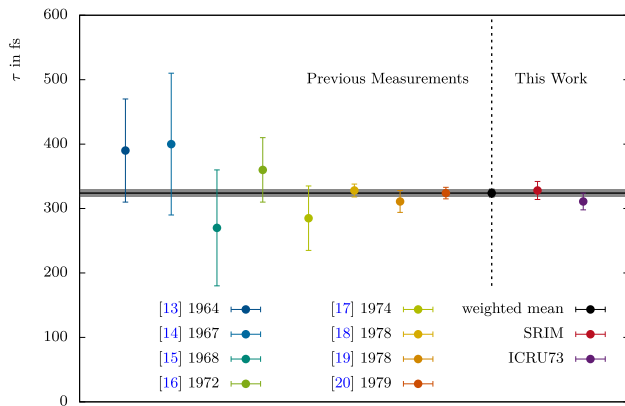


**Fig. 3** Temporal development of the measured lifetimes for the  $4_1^+$  state in  $^{22}\text{Ne}$ . The eight values from the previous measurements are taken from [13–20] respectively. They lead to the uncertainty weighted mean of 324(6)fs [21], which is shown as a black point and as a grey uncertainty band. The results from this work, illustrated by the red (SRIM stopping powers) and purple (ICRU73 stopping powers) data points, are in excellent agreement with the previous measurements

### 2.1 Lifetime of the $2_2^+$ state

In order to access the  $2_2^+$  state, we need to look at an even more selective channel, i.e., the 2p gated  $\gamma$  rays in coincidence with the  $2_1^+ \rightarrow 0_{g.s.}^+$   $\gamma$ -ray transition of  $^{16}\text{C}$ . Figure 4 shows the  $\gamma$ -ray spectra in coincidence with the  $2_1^+ \rightarrow 0_{g.s.}^+$  transition for Gammasphere angles from  $69.82^\circ$  to  $162.73^\circ$ . For smaller angles no transitions of  $^{16}\text{C}$  could be observed with certainty. The three dashed lines in the spectra mark the expected center-of-mass energy for the three transitions  $4_1^+ \rightarrow 2_1^+$ ,  $3_1^+ \rightarrow 2_1^+$  and  $2_2^+ \rightarrow 2_1^+$ , which all feed the  $2_1^+$  state (see Fig. 1). In Fig. 4 one clearly sees the  $4_1^+ \rightarrow 2_1^+$  transition

as a stopped peak for most angles. The  $2_2^+ \rightarrow 2_1^+$  transition could be observed as a moving peak for six angles. The red fit-functions at the  $2_2^+ \rightarrow 2_1^+$  transition peaks in Fig. 4 are defined by a single Gaussian function using the binned-likelihood method recommended in case of low statistics; same results are obtained using the center of gravity approach. The results for the mean value of these fits are plotted against  $\cos(\theta)$  in Fig. 5, where  $\theta$  is the central angle of the Gammasphere detectors.<sup>1</sup> The fit, described by

$$E_{\text{Lab}}(\bar{\beta}, \theta) = E_{\text{cm}} \frac{\sqrt{1 - \bar{\beta}^2}}{1 - \bar{\beta} \cos \theta}, \tag{1}$$

yields  $E_{\text{cm}} = 2213(4)$  keV, in agreement with the uncertainty weighted mean value of 2217(2) keV from [6, 8], and  $\bar{\beta}_{\text{Exp}} = 0.03905(245)$  for the mean decay velocity.

In order to draw any conclusion on the lifetime of the state using the mean velocity of the decay ( $\bar{\beta}_{\text{Exp}}$ ), we need to know the initial velocity of the excited  $^{16}\text{C}$  ions. Although one could calculate this velocity from the fusion-evaporation reaction dynamics, this does not take into account the experimental conditions, e.g., detection angles, proton detection efficiency, etc. We therefore determined this initial velocity experimentally. To achieve this, a similar measurement albeit using a very thin (0.093 mg/cm<sup>2</sup>), self-supporting  $^9\text{Be}$  target was performed. By fitting the laboratory  $\gamma$ -ray energy as a function of  $\cos(\theta)$  of the strongly populated  $2_1^+ \rightarrow 0_{g.s.}^+$  transition (as similarly done in Fig. 5), we extract the mean velocity of the decay. The energy loss in such thin target is negligible and therefore the velocity of the particle during the decay is approximately the same as the velocity the particle has directly after its creation. The latter was determined to be  $\bar{\beta}_{\text{TO}} = 0.04527(44)$  (TO stands for target-only runs, i.e., no degrader). This method has the advantage that all systematics of the experimental setup are already included in the extracted mean velocity  $\bar{\beta}$ , such as systematic effects of proton losses in the target, the response of the Microball and Gammasphere detectors, and the fusion-evaporation kinematics. The response of Microball is particularly important as it is strongly angle dependent due to, e.g., different absorbers used at each Microball angle.

To extract the lifetime of the state from the determined velocities at the time of creation<sup>2</sup> and the decay velocity,<sup>3</sup> we employ Geant4 to simulate the slowing-down process and study the decay of the state of interest through the same

<sup>1</sup> We performed Monte Carlo simulations to find the average angle (as opposed to the central angle)  $\theta$ . The difference is very small and the results remain robust; the maximum difference between the central angle and average angle is 0.4 degrees, and the maximum difference of the cosine of the central angle, the cosine of the average angle, and the average of cosine angle is of the order  $10^{-3}$ .

<sup>2</sup>  $\bar{\beta}_{\text{TO}} = 0.04527(44)$ .

<sup>3</sup>  $\bar{\beta}_{\text{Exp}} = 0.03905(245)$ .

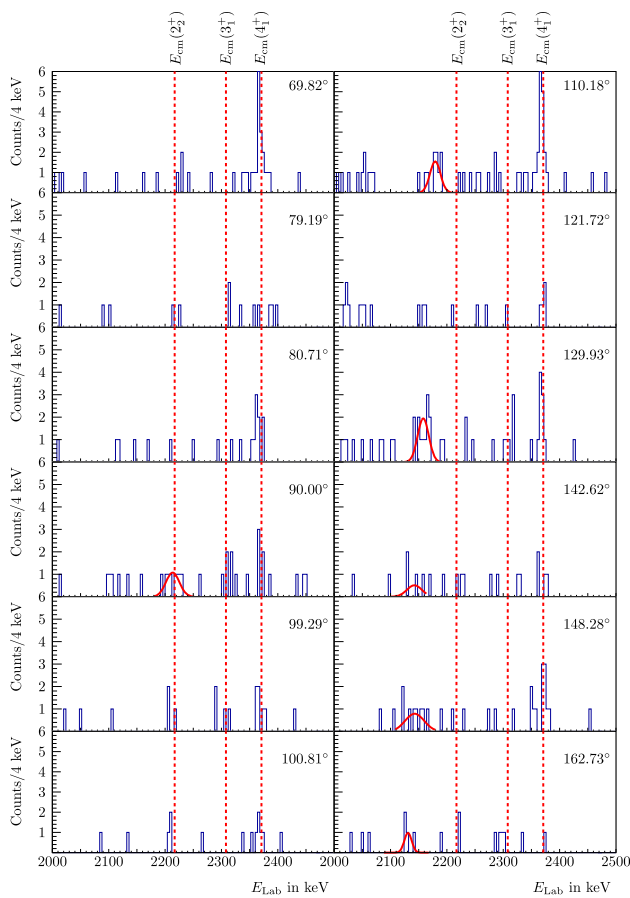


**Fig. 4** Gamma-ray spectra in coincidence with the  $2_1^+ \rightarrow 0_{g.s.}^+$  transition for Gammasphere angles from  $69.82^\circ$  to  $162.73^\circ$  and a  $2\sigma$  coincidence in Microball. The spectra for the discrete Gammasphere angles are obtained for a  $2\sigma$   $\gamma$  gate on the  $2_1^+ \rightarrow 0_{g.s.}^+$  transition with  $E_{cm} = 1760$  keV and  $\sigma = 3.2$  keV. The red dashed lines mark the expected center-of-mass energies for the  $4_1^+ \rightarrow 2_1^+$  ( $E_{cm}(4_1^+)$ ),  $3_1^+ \rightarrow 2_1^+$  ( $E_{cm}(3_1^+)$ ) and  $2_2^+ \rightarrow 2_1^+$  ( $E_{cm}(2_2^+)$ ) transitions [6,8]. The red fit-functions are defined by a single Gaussian function using the binned-likelihood method recommended in case of low statistics

target/degrader material budget as in the experiment for various lifetimes. Indeed, we simulated excited  $^{16}\text{C}$  ions using their initial velocity  $\bar{\beta}_{\text{TO}}$  and taking into account the thickness of the target ( $1.38 \text{ mg/cm}^2$ ), how the latter affects the fusion-evaporation cross section and how the  $\bar{\beta}_{\text{TO}}$  would turn into a distribution of initial velocities according to where the  $^{16}\text{C}$  ions were created along the target thickness.

An important parameter in our simulations that will affect the lifetime of the state is the stopping powers that are employed by Geant4. The standard database used by Geant4 for energy loss of ions in matter is the ICRU73 dataset, which includes a mixture of calculated and measured stopping powers for ions heavier than helium [22]. Geant4 is developed and optimized for high-energy experiments. Following the investigations of [23], two changes in the simulation process are applied to get a more accurate slowing down behaviour of

ions at low energies. First, the ICRU73 stopping powers are replaced by stopping powers which are calculated with the program SRIM, a software-package which reproduces well the stopping behaviour of ions for different materials over a wide energy range [24]. Secondly, the so-called *forced stepping* method is added to the simulation code, where the simulation evaluates the behaviour of the particle no later than a given distance set by the user. The *forced stepping* distance should be set to small values for low-energy physics, as is done in this work.

The simulation was performed for various lifetimes of the  $2_2^+$  state and the results were analyzed much in the same way as was done with the experimental data, i.e., the mean-decay velocity was extracted by plotting the laboratory energy versus the  $\cos(\theta)$  as in Fig. 5. The resulting mean decay velocities from the simulations,  $\bar{\beta}_{\text{Sim}}$ , as a function of simulated lifetimes are shown in Fig. 6. The intersection between the simulated results and the experimentally defined velocity  $\bar{\beta}_{\text{Exp}}$ , and in particular the upper limit of the uncertainty band, defines the lower limit of the lifetime. This results in  $\tau \gtrsim 244$  fs for SRIM stopping powers for the  $2_2^+$  state.

To constrain the lifetime of the  $2_2^+$  state further, an additional evaluation method is applied to the data. The number of counts in the moving-peak component ( $C_{\text{Moving}}$ ) are compared to the number of counts in the stopped-peak component ( $C_{\text{Stopped}}$ ). The longer the lifetime of the state, the more decays take place at rest and therefore the stopped-peak component increases. For the evaluation of the  $2_2^+$  state, Geant4 simulations are performed for different lifetimes and the ratio

$$R_{\text{Sim}}(\tau_{\text{Sim}}) = \frac{C_{\text{Stopped}}(\tau_{\text{Sim}})}{C_{\text{Moving}}(\tau_{\text{Sim}})} \quad (2)$$

is calculated for different lifetimes and for each Gammasphere angle separately. Then the following function is fitted

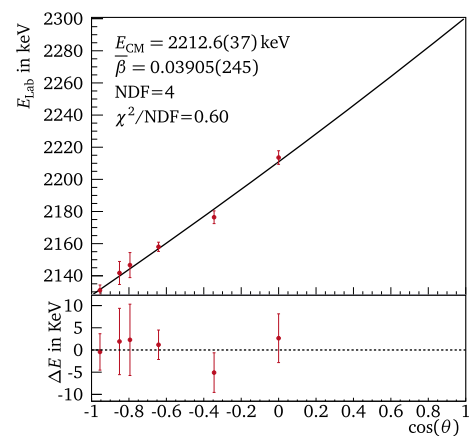


**Fig. 5**  $E_{\text{Lab}}$  versus  $\cos(\theta)$  fit for the  $2_2^+ \rightarrow 2_1^+$  transition of  $^{16}\text{C}$ . The  $E_{\text{Lab}}$  values are extracted from the Gaussian fits shown in Fig. 4. The black fit-function is described by Eq. 1. The lower plot shows the residuals  $\Delta E$  of the fit which is shown in the upper part

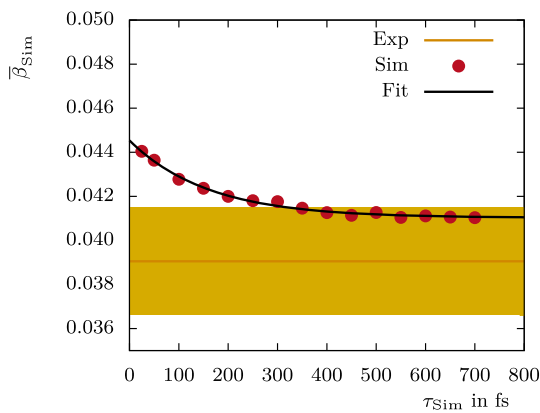


**Fig. 6** Simulated mean decay beta  $\bar{\beta}_{Sim}$  versus simulated lifetime  $\tau_{Sim}$  for the  $2_2^+ \rightarrow 2_1^+$  transition of  $^{16}\text{C}$ . The initial beta in the simulation was obtained with  $\bar{\beta}_{TO} = 0.04527(44)$ . The yellow band illustrates the experimental mean decay beta value of  $\bar{\beta}_{Exp} = 0.03905(245)$  including its uncertainty

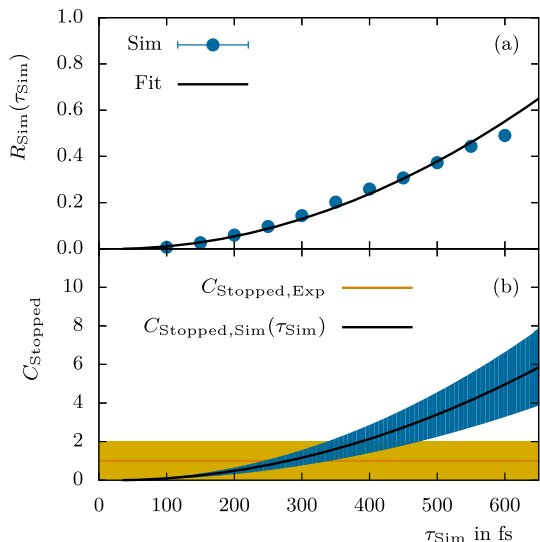


**Fig. 7** **a** Ratio of counts between the moving and stopped peak component for the  $2_2^+ \rightarrow 2_1^+$  transition of  $^{16}\text{C}$  for  $110.18^\circ$  and results from the Geant4 simulations with Eq. 3 as a fit-function. **b** This fit-function scaled with  $C_{Moving,Exp}$ , which represents  $C_{Stopped,Sim}(\tau_{Sim})$ . The blue band around the function shows its uncertainty including the uncertainty from  $C_{Moving,Exp}$  as well as the fit uncertainties. Also  $C_{Stopped,Exp} = 1(1)$  counts is plotted in orange for which the uncertainty is shown as a yellow band

to the simulated data, as shown in Fig. 7a,

$$R_{Sim}(\tau_{Sim}) = a \cdot \tau_{Sim}^2 + b \cdot \tau_{Sim}. \tag{3}$$

The number of counts in the moving-peak component in the experimental data ( $C_{Moving,Exp}$ ) is used to deduce how many counts should appear in the simulated stopped-peak component ( $C_{Stopped,Sim}$ ) for a given lifetime:

$$C_{Stopped,Sim}(\tau_{Sim}) = C_{Moving,Exp} \cdot R_{Sim}(\tau_{Sim}). \tag{4}$$

The result for  $110.18^\circ$  is shown as a black function in Fig. 7b. The blue band around the function shows its uncertainty, i.e., the uncertainty from  $C_{Moving,Exp}$  as well as the fit uncertainties. By comparing the experimental number of counts  $C_{Stopped,Exp}$  for the stopped-peak component with  $C_{Stopped,Sim}(\tau_{Sim})$ , we get an upper limit for the lifetime of the  $2_2^+$  state. The horizontal (orange) line with yellow band in Fig. 7b shows the experimental result for the stopped-peak component of  $C_{Stopped,Exp} = 1(1)$  counts. Here, the mean value from  $C_{Stopped,Exp}$ , including its uncertainty  $u(C_{Stopped,Exp})$ , can be seen as an upper limit for the number of counts in the stopped-peak component, which is still compatible with the experimental data. Hence, all lifetimes for which the blue and yellow area are overlapping are compatible with the experimental data. Due to this, an upper lifetime limit is obtained by determining the intersection between  $C_{Stopped,Sim}(\tau_{Sim}) + u[C_{Stopped,Sim}(\tau_{Sim})]$  (right end of the blue uncertainty band) and  $C_{Stopped,Exp} + u[C_{Stopped,Exp}]$  (upper border of the yellow uncertainty band).

For this analysis only the spectra for  $110.18^\circ$  and  $129.93^\circ$  Gammasphere angles are used to reduce statistical uncertainties; these are the only spectra for which we have significant number of counts in the moving-peak component. In addition, in these angles the moving- and stopped-peak component do not overlap, reducing further experimental uncertainties. The analysis is done separately for the  $110.18^\circ$  and  $129.93^\circ$  data and the results are combined by calculating the corresponding mean value. The analysis was also repeated for the extreme target thicknesses to include the target thickness uncertainties in the results. The lifetimes are always longer for the thickest possible target (+10% thickness). Hence, these results are used as a systematic uncertainty for the upper lifetime limit. The latter is  $\gamma$ -ray energy dependent and results to an upper lifetime limit of 376 fs for a center-of-mass transition energy between 2209.0 keV and 2213.5 keV and 446 fs for a center-of-mass transition energy between 2213.5 keV and 2217.0 keV;  $E_{cm} = 2213(4)$  keV as extracted in Fig. 5. We have assumed no background in the  $\gamma$ -ray spectrum and the upper lifetime limit is determined at 70% confidence level (C.L.); the C.L. is expected to change, becoming higher or lower, if random background is present in the energy region of the stopped and/or moving component, respectively, see, e.g., [25].

Figure 8 summarizes the results for the lifetime of the  $2_2^+$  of  $^{16}\text{C}$ . Using SRIM stopping powers and taking the systematic uncertainties into account, the lifetime can be expected in a range from 244 fs to 376 fs for a center-of-mass transition energy between 2209.0 keV and 2213.5 keV and the lifetime can be expected in a range from 244 fs to 446 fs for a center-of-mass transition energy between 2213.5 keV and 2217.0 keV. In Fig. 8 results from Ciemała et al. [7] are also shown. The figure shows the upper lifetime limit (black dashed horizontal line) from the count ratio method

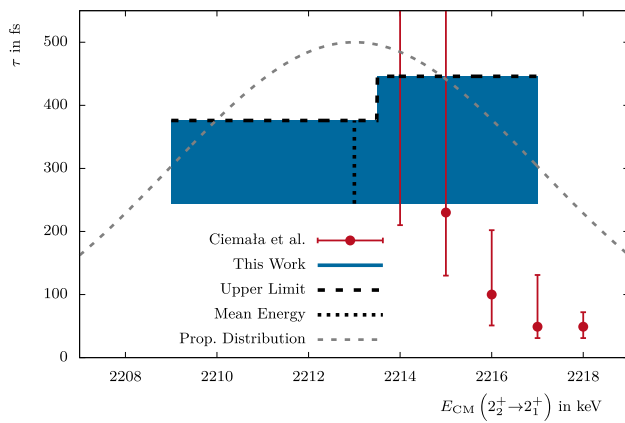


**Fig. 8** Results for the lifetime range of the  $2_2^+$  state in  $^{16}\text{C}$  using the count ratio method and SRIM stopping powers. The values from this work are shown as black dashed lines and blue boxes. The horizontal black dashed lines mark the upper lifetime limit while the vertical black dashed line marks the mean  $\gamma$ -ray energy for the  $2_2^+ \rightarrow 2_1^+$  transition as measured in this work. The blue boxes mark the most likely lifetime range. The external values shown as red dots are the most recent measurements from Ciemała et al. [7]. The grey dashed function shows the relative probability distribution as a function of the transition energy for our results. It follows a Gaussian distribution with a mean of 2213 keV and a sigma of 4 keV

and the most likely lifetime range (blue boxes) using the estimated lower lifetime from the mean decay beta method. The results from Ciemała et al. are marked by the red data points. According to Ciemała et al. the transition energy should be located between 2214 and 2218 keV and the lifetime depends strongly on this energy as can be seen in Fig. 8. Comparing both results, this work suggests a transition energy which is slightly lower than the energy measured by Ciemała et al. In terms of lifetimes, the data points from 2214 keV and 2215 keV are in agreement with the most likely lifetime range from this work. The other data points from Ciemała et al. are lower than the most likely lifetime range from this work.

## 2.2 Lifetime of the $4_1^+$ state

Figure 2 shows that the  $4_1^+ \rightarrow 2_1^+$  transition presents a significant stopped peak, corresponding to a longer lifetime (in the picosecond range) than this method is sensitive to. Therefore, we can only put a lower limit to the lifetime of the  $4_1^+$  state. Additionally, from Ref. [8] it is already known that the lifetime of the  $4_1^+$  state should be faster than 4 ps. We can then constrain theoretical calculations by using the range of lifetimes as extracted from this experiment and previous works.

To achieve a proper lower lifetime limit, the experimental  $\gamma$ -ray spectra for each Gammasphere angle are compared to Geant4 simulations. As we discussed in the previous section, the ratio between the stopped and moving component of a  $\gamma$  ray depends strongly on the lifetime of the decaying state. To infer the lower limit of the lifetime of the  $4_1^+$  state, we

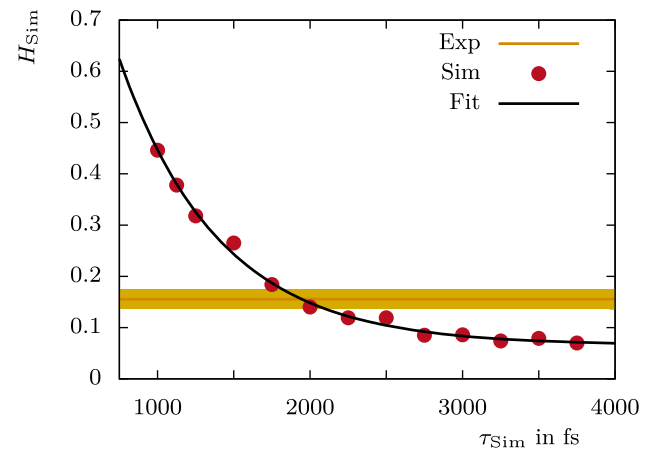


**Fig. 9** Estimation of a lower lifetime limit for the  $4_1^+$  state of  $^{16}\text{C}$  using the  $148.28^\circ$  Gammasphere spectrum. Geant4 simulation results for  $H_{\text{Sim}}(\tau_{\text{Sim}})$  have been performed using SRIM stopping powers and  $\bar{\beta}_{\text{TO}} = 0.04527(44)$ . The black fit-function is described by Eq. 7. The yellow band illustrates the experimental ratio of  $H_{\text{Exp}} = 0.156(19)$  including its uncertainty

look at the ratio of these two peaks in our experiment (in coincidence with two protons detected in Microball) and we compare this with our simulations.

First we investigate whether we have a moving peak in our experimental spectrum. For this purpose a peak on top of the background has to have a maximum height which is larger than the  $2\sigma$  uncertainty of the background. Everything else is considered as background fluctuations. The  $2\sigma$  uncertainty of the background will be labelled as  $M_{\text{BG}}$  hereafter. Additionally, the maximum height of the stopped peak  $M_{\text{Stopped}}$  from the  $4_1^+ \rightarrow 2_1^+$  transition is extracted to calculate the ratio

$$H_{\text{Exp}} = \frac{M_{\text{BG}}}{M_{\text{Stopped}}} \quad (5)$$

This is performed for those Gammasphere angles for which the  $4_1^+ \rightarrow 2_1^+$  transition is resolved clearly in the spectrum, i.e.,  $121.72^\circ$ ,  $129.93^\circ$ ,  $142.62^\circ$ ,  $148.28^\circ$ , and  $162.73^\circ$ . For smaller angles the  $4_1^+ \rightarrow 2_1^+$  transition interferes with the  $7/2_1^+ \rightarrow 5/2_1^+$  transition of  $^{15}\text{N}$  and cannot be used in the analysis.

The  $4_1^+ \rightarrow 2_1^+$  transition is simulated for different lifetimes of the  $4_1^+$  state and the ratio

$$H_{\text{Sim}}(\tau_{\text{Sim}}) = \frac{M_{\text{Moving}}}{M_{\text{Stopped}}} \quad (6)$$

is calculated for each simulated lifetime  $\tau_{\text{Sim}}$ , where  $M_{\text{Moving}}$  is the peak maximum of the moving peak component and  $M_{\text{Stopped}}$  is the peak maximum of the stopped peak component. A function of the form

$$H_{\text{Sim}}(\tau_{\text{Sim}}) = a \cdot e^{-b\tau_{\text{Sim}}} + c \quad (7)$$

is then fitted to the simulated data.

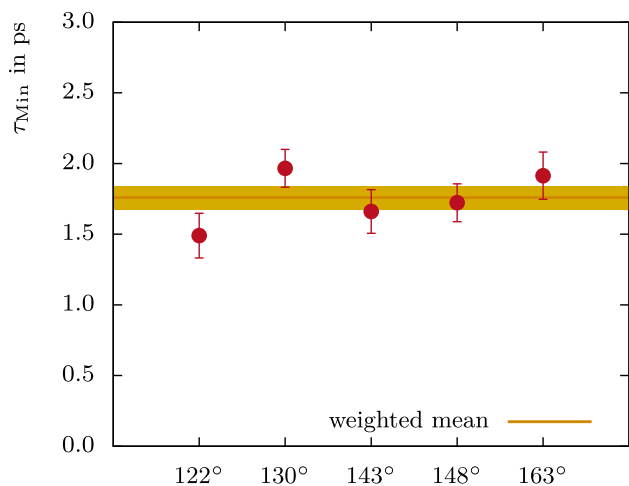


**Fig. 10** Results for a lower lifetime limit  $\tau_{\text{Min}}$  for the  $4_1^+$  state of  $^{16}\text{C}$ . The Geant4 simulations were performed for  $\bar{\beta}_{\text{TO}} = 0.04527(44)$ . The yellow band illustrates the uncertainty weighted mean including its  $1\sigma$  uncertainty for these data points. The uncertainty weighted mean is deduced to 1.95(9)ps for SRIM stopping powers

In Fig. 9 this is shown for the  $148.28^\circ$  Gammasphere angle. To obtain a lower lifetime limit,  $\tau_{\text{Min}}$ , we use the intersection of the fit-function with the experimental ratio  $H_{\text{Exp}}$ . In the figure this is visualized by the intersection of the black fit-function and the orange line which represents the experimental ratio  $H_{\text{Exp}}$ . The yellow band around the line represents its statistical uncertainty.

The final result was extracted as the uncertainty weighted mean from all five Gammasphere angles, see Fig. 10, to be 1.95(9)ps and this yields a lower lifetime limit of  $\tau_{\text{Min}} = 1.9\text{ps}$  by subtracting the mean value by its  $1\sigma$  uncertainty. Additionally, systematic uncertainties due to the target thickness<sup>4</sup> yield the final result of  $\tau_{\text{Min}} = 1.9^{+0.0}_{-0.1}(\text{syst}_{\text{target}})\text{ps}$  as a lower lifetime limit for the  $4_1^+$  state of  $^{16}\text{C}$ .

Combining the present results with the upper lifetime limit from Ref. [8], the lifetime of the  $4_1^+$  state is between 1.8 ps and 4 ps which corresponds to a decay rate of  $\lambda_{\text{Min}}(4_1^+) = 2.50 \cdot 10^{11} \frac{1}{\text{s}}$  and  $\lambda_{\text{Max}}(4_1^+) = 5.55 \cdot 10^{11} \frac{1}{\text{s}}$ . Using the experimental transition energy of 2369 keV, the  $E2$  transition strength of the  $4_1^+ \rightarrow 2_1^+$  state is

$$2.74 \text{ e}^2\text{fm}^4 \leq B(E2; 4_1^+ \rightarrow 2_1^+) \leq 6.10 \text{ e}^2\text{fm}^4. \quad (8)$$

### 3 Theory

Electromagnetic transitions in  $^{16}\text{C}$  are a particular challenge for ab initio nuclear structure theory. On the one hand, this

<sup>4</sup> The same analysis was performed using a 10% thinner target which would yield a shorter lifetime.

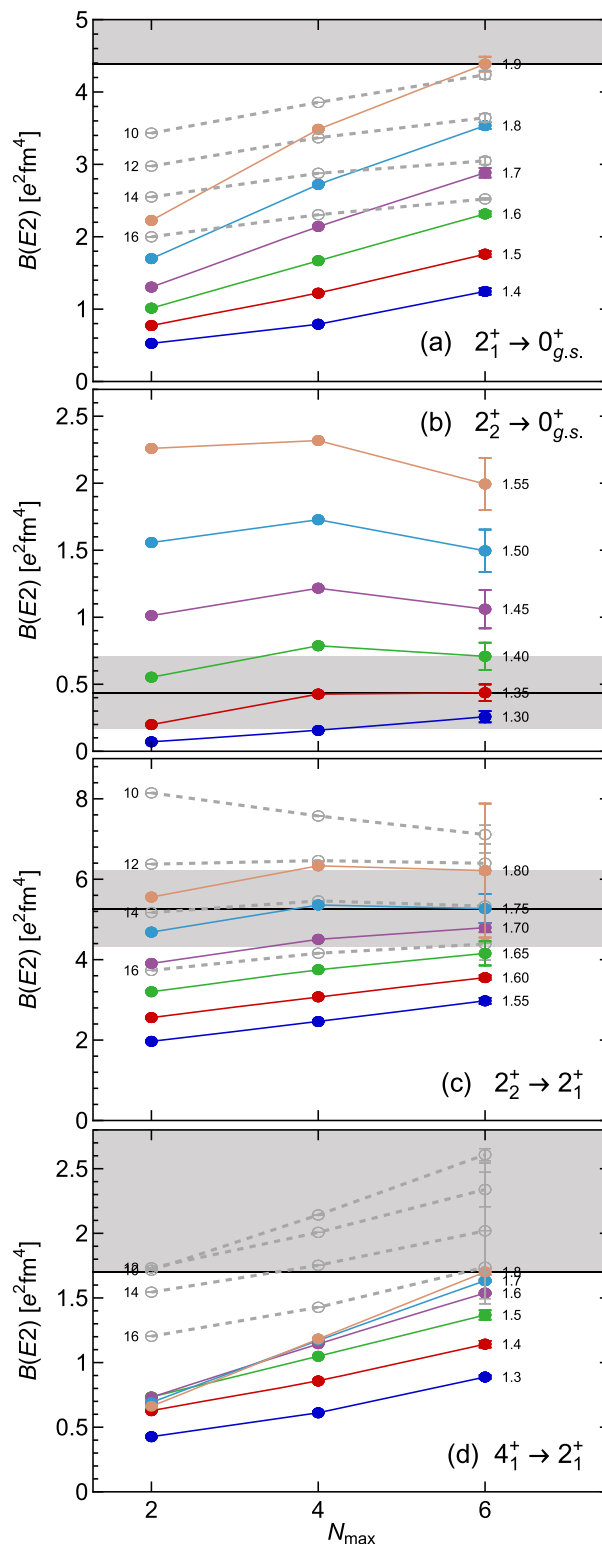


**Fig. 11** Results of ab initio NCSM calculations for the  $B(E2)$  transition strengths involving the  $0^+$  ground state, the first two  $2^+$  excited states, and the first  $4^+$  excited state. The colored symbols show the  $N_{\text{max}}$  dependence obtained with the SNAT basis for different values of  $a_{\text{SNAT}}$  [fm] as indicated on the right-hand-side of each sequence. The grey symbols show  $N_{\text{max}}$  sequences obtained with the HO basis for different values of  $\hbar\Omega$  [MeV] as indicated on the left-hand-side of each sequence

nucleus is at the upper end of the mass range where conventional ab initio methods, such as the NCSM, can be applied. Moreover,  $E2$  observables exhibit a notoriously slow convergence, so that precise converged calculations, e.g., for  $B(E2)$  strengths, are beyond our computational capabilities. On the other hand, recent ab initio approaches for medium-mass nuclei, such as the in-medium similarity renormalization group (IM-SRG) and its open-shell extensions, e.g., the valence-space IM-SRG [26,27] and the in-medium NCSM [28], overcome the convergence limitations for ground-state and excitation energies but exhibit deficiencies in the description of  $E2$  observables. For the valence-space IM-SRG it was shown that  $B(E2)$  transition strengths are severely underestimated in present calculation due to missing three- and multi-body terms in the IM-SRG evolution of the  $E2$  operator [29]. In the in-medium NCSM, which uses multi-reference IM-SRG evolved operators for a subsequent NCSM calculation in small model spaces, the situation is more subtle. For some transitions, e.g., the  $2_1^+$  to ground-state transition in  $^{12}\text{C}$ , the in-medium NCSM provides precise results, but for the corresponding transition in  $^{16}\text{C}$  the  $B(E2)$  is drastically underestimated. Work is under way to fix these limitations by, e.g., extension of the IM-SRG to three-body operators or by tailoring the reference space in the in-medium NCSM to capture all of the relevant collective correlations.

In this work we limit ourselves to direct NCSM calculations for  $^{16}\text{C}$ . In order to improve the convergence, particularly of long-range observables like the  $E2$ , we use a generalized natural-orbital basis instead of the conventional harmonic-oscillator single-particle basis. The natural orbitals as introduced in Ref. [30] have proven extremely useful in connection with the NCSM and other many-body methods—they optimize the model-space convergence and remove the dependence on the oscillator frequency or oscillator length. While this is advantageous for NCSM calculations of energies, a parameter that controls the length scale of the basis is advantageous to assess the convergence systematics in cases where full convergence cannot be reached. Therefore, we use a scaled version of the natural-orbital (SNAT) basis in this work. Starting with a natural orbital basis constructed for a nominal oscillator length of  $a_{\text{HO}} = 1.4$  fm we scale all single-particle wave functions to a different length parameter  $a_{\text{SNAT}}$ , the ratio  $a_{\text{SNAT}}/a_{\text{HO}}$  defines the scaling factor by which the wavefunctions are stretched radially. We perform NCSM calculations for a set of length parameters  $a_{\text{SNAT}}$  and analyze the convergence pattern of the full set.

For all calculations we use state-of-the-art chiral NN+3N interactions at next-to-next-to-next-to-leading order ( $\text{N}^3\text{LO}$ ) for both the NN and the 3N contributions. This interaction has been introduced in Ref. [31] and provides an excellent description of ground-state energies and charge radii up into the medium-mass regime. We use a free-space SRG transformation of the Hamiltonian and all other operators

with  $\alpha = 0.08$  fm<sup>4</sup> [32,33]. Since we are dealing with non-converged NCSM calculations, the many-body uncertainties are dominant for the observables discussed here. Therefore, we do not explicitly include the uncertainty estimated for the chiral truncation and we also omit chiral two-body corrections to the  $E2$  operator.

In Fig. 11 we present the convergence patterns for various  $B(E2)$  transition strengths in  $^{16}\text{C}$  involving the  $0^+$  ground state, the first two  $2^+$  excited states, and the first  $4^+$  excited state. The colored symbols represent different length parameters  $a_{\text{SNAT}}$  of the SNAT basis as indicated on the right-hand end of the individual  $N_{\text{max}}$  sequences. In cases where the HO basis calculations show a different overall trend, we also show  $N_{\text{max}}$  sequences for four different HO frequencies, as denoted on the left-hand side of the data sequences, for comparison.

The  $N_{\text{max}}$  sequences for the different transitions show the notorious problem with  $E2$  observables in NCSM and other ab initio calculations: they exhibit an extremely slow convergence. None of the calculations shown can be considered fully converged. Moreover, extrapolations to the infinite Hilbert space are difficult and strongly model dependent. Therefore, we take a pragmatic approach and assess the overall convergence pattern and try to estimate the  $B(E2)$  for the SNAT basis for an optimal  $a_{\text{SNAT}}$  length parameter. In two cases, the  $2_2^+ \rightarrow 0_{g.s.}^+$  and the  $2_2^+ \rightarrow 2_1^+$  transitions, we can identify an optimal value for  $a_{\text{SNAT}}$  that leads to a constant result for the  $B(E2)$  in the two largest model spaces. The maximum difference to the neighboring two  $a_{\text{SNAT}}$  for the largest  $N_{\text{max}}$  is used as an uncertainty estimate. These estimates are indicated in panels (b) and (c) of Fig. 11 by black horizontal lines with a grey band indicating the uncertainty, the numerical values are summarized in Table 1. This selection is supported by the general trend of the other sequences, which all move towards the estimated value. For the other two cases, the  $2_1^+ \rightarrow 0_{g.s.}^+$  and the  $4_1^+ \rightarrow 2_1^+$  transition, the calculations for all  $a_{\text{SNAT}}$  and  $\hbar\Omega$  show a monotonic increase with  $N_{\text{max}}$ . Therefore, within the range of basis parameters used here, we cannot estimate the  $B(E2)$  as for the other cases, we can only specify a lower bound given by the maximum value of the  $B(E2)$  obtained in the calculations, which is again indicated by a black line in panels (a) and (d) of Fig. 11.

## 4 Discussion

We will now discuss how our experimental findings compare with the new ab initio calculations described in Sect. 3. In Table 1 we summarize the experimental values for the energy of the  $2_1^+$ ,  $2_2^+$ ,  $4_1^+$  states in  $^{16}\text{C}$ , their lifetimes, the branching ratio of the  $\gamma$ -ray decay of the  $2_2^+$  state from [6], the transition

strengths that are implied from the lifetimes of the states, and how they compare with theoretical calculations.

For the  $2_1^+ \rightarrow 0_{g.s.}^+$  and  $4_1^+ \rightarrow 2_1^+$  transitions, the lifetime can be translated into a  $B(E2)$  transition strength directly. However, the  $2_2^+$  state can decay via the  $2_2^+ \rightarrow 0_{g.s.}^+$  and the  $2_2^+ \rightarrow 2_1^+$  transition. For the  $2_2^+ \rightarrow 0_{g.s.}^+$  transition only an  $E2$  component is possible. For the  $2_2^+ \rightarrow 2_1^+$ , both  $M1$  and  $E2$  decay modes can dominate. Therefore, the lifetime of the  $2_2^+$  state,  $\tau(2_2^+) = [244, 446]$  fs, can be translated into the total decay rate and compared with theory. The total decay rate of the  $2_2^+$  state,  $\lambda_{\text{Total}}(2_2^+)$ , is

$$\lambda_{\text{Total}}(2_2^+) = \lambda(E2; 2_2^+ \rightarrow 0_{g.s.}^+) + \lambda(E2; 2_2^+ \rightarrow 2_1^+) + \lambda(M1; 2_2^+ \rightarrow 2_1^+) = 1/\tau(2_2^+) \tag{9}$$

with

$$2.25 \cdot 10^{12} \text{ s}^{-1} \leq \lambda_{\text{Total}}(2_2^+) \leq 4.10 \cdot 10^{12} \text{ s}^{-1}. \tag{10}$$

From [6] it is also known that the branching ratio for the  $2_2^+ \rightarrow 0_{g.s.}^+$  transition is limited to

$$\text{BR}(2_2^+ \rightarrow 0_{g.s.}^+) = \frac{\lambda(E2; 2_2^+ \rightarrow 0_{g.s.}^+)}{\lambda_{\text{Total}}(2_2^+)} < 8.8 \%. \tag{11}$$

From Eqs. (10) and (11) we obtain an upper limit for the  $E2$  strength of the  $2_2^+ \rightarrow 0_{g.s.}^+$  transition of

$$B(E2; 2_2^+ \rightarrow 0_{g.s.}^+) < 0.30 \text{ e}^2\text{fm}^4. \tag{12}$$

The total decay rate (Eq. (9)) of the  $2_2^+$  state can be expanded as

$$\begin{aligned} \lambda_{\text{Total}}(2_2^+) &= \frac{1.22 \cdot 10^9}{\text{s}} \left( \frac{E_\gamma(2_2^+ \rightarrow 0_{g.s.}^+)}{\text{MeV}} \right)^5 \frac{B(E2; 2_2^+ \rightarrow 0_1^+)}{\text{e}^2\text{fm}^4} \\ &+ \frac{1.22 \cdot 10^9}{\text{s}} \left( \frac{E_\gamma(2_2^+ \rightarrow 2_1^+)}{\text{MeV}} \right)^5 \frac{B(E2; 2_2^+ \rightarrow 2_1^+)}{\text{e}^2\text{fm}^4} \\ &+ \frac{1.76 \cdot 10^{13}}{\text{s}} \left( \frac{E_\gamma(2_2^+ \rightarrow 2_1^+)}{\text{MeV}} \right)^3 \frac{B(M1; 2_2^+ \rightarrow 2_1^+)}{\mu_N^2}. \end{aligned} \tag{13}$$

By combining this with the experimentally known transition energies and the constraints from Eqs. (10) and (12), one can deduce an explicit constraint on the three transition strengths.

We can now confront the NCSM calculation with this experimental information. The ab initio results obtained with the new generation of chiral NN+3N interactions are compatible with the experimental data for all observables for the first time. Previous NCSM calculations reported in Ref. [5], which are based on the the CD Bonn 2000 phenomenological NN interaction without an initial 3N force, fail to reproduce the experimental pattern of  $B(E2)$  values. As illustrated in Table 1, the  $B(E2)$  value for the  $2_1^+ \rightarrow 0_{g.s.}^+$  transition is

underestimated and the  $B(E2)$  for the  $2_2^+ \rightarrow 0_{g.s.}^+$  transition is overestimated significantly. This leads to an underestimation of the lifetime of the  $2_2^+$  state and the branching ratio for the  $2_2^+ \rightarrow 2_1^+$  transition by a factor of 3.

The chiral NN+3N interaction at  $N^3\text{LO}$  used in the present NCSM calculations predicts a large value for the  $2_1^+ \rightarrow 0_{g.s.}^+$  transition and a small value for the  $2_2^+ \rightarrow 0_{g.s.}^+$  transition in good agreement with experiment. The resulting total transition rate obtained from Eq. (13) and, thus, the lifetime of the  $2_2^+$  state are in excellent agreement with experiment when using the experimental transition energies. Stated differently, the transition strengths obtained in the calculation fulfill the constraints provided by the experimental data via Eq. (13). Using the calculated transition energies from the NCSM we still find a good agreement of the  $2_2^+$  lifetime with experiment. It is important to note that the calculated excitation energies agree with experiment within uncertainties, however, the lifetime is very sensitive to transition energies and thus amplifies their theory uncertainties. The branching ratio for the  $2_2^+ \rightarrow 2_1^+$  transition is also in good agreement with experiment irrespective of the choice of energies. In addition, the lower bounds derived from the NCSM sequences for the  $B(E2)$  of the  $2_1^+ \rightarrow 0_{g.s.}^+$  and the  $4_1^+ \rightarrow 2_1^+$  transition are compatible with the experimental data, thus providing a consistent description of the complete spectroscopy of these states.

The calculations presented in Ref. [5] also included results for a first generation of chiral NN+3N interactions using a local 3N interaction at  $N2\text{LO}$ . Though these calculations were not converged and only ratios of  $B(E2)$  transition strengths were discussed, some important features were observed. Most notably, the suppression of the  $B(E2)$  for the  $2_2^+ \rightarrow 0_{g.s.}^+$  through the inclusion of the 3N interaction. The same mechanism is at play for the new-generation chiral NN+3N interactions used in this work. However, the first-generation NN+3N interaction produces significantly smaller absolute values, e.g., for the  $B(E2)$  for the  $2_1^+ \rightarrow 0_{g.s.}^+$  transition. Comparing results at fixed  $N_{\text{max}} = 6$ , the  $B(E2)$  obtained in Ref. [5] is about 50% smaller and, thus, incompatible with experiment. This is in line with the general observation that the first-generation chiral NN+3N interactions produce too small radii starting from the mid p-shell. This deficiency has been fixed in the new-generation of interactions and translates to larger  $E2$  strength.

### 5 Summary

Meaningful limits to the lifetimes of higher-lying excited states in  $^{16}\text{C}$  were extracted in order to benchmark ab initio calculations. Indeed, the structure of  $^{16}\text{C}$  has been highlighted as an important touchstone for these calculations,

**Table 1** Level energies ( $E$ ), lifetimes ( $\tau$ ), transition strengths ( $B(E/M)$ ), total decay rates ( $\lambda_{\text{Total}}$ ) and branching ratios (BR) for  $^{16}\text{C}$  from this work (unless a reference is provided), and how they compare with theory (see text for details)

State		Experiment	NCSM NN+NNN		NCSM CDB2k [5]		Unit
$2_1^+$	$E(2_1^+)$	$1759.0 \pm 0.4$	$1650 \pm 100$		$2430 \pm 50$		keV
	$B(E2; 2_1^+ \rightarrow 0_{g.s.}^+)$	$4.1_{-0.3}^{+0.5}$ [6, 8, 34]	$> 4.39$		$2.2 \pm 0.9$		$\text{e}^2\text{fm}^4$
$2_2^+$	$E(2_2^+)$	$3972 \pm 4$	$4200 \pm 250$		$4900 \pm 300$		keV
	$B(E2; 2_2^+ \rightarrow 2_1^+)$	Eqs. (10), (13)	$5.27 \pm 0.95$		$4.4 \pm 1.8$		$\text{e}^2\text{fm}^4$
	$B(M1; 2_2^+ \rightarrow 2_1^+)$	Eqs. (10), (13)	$0.012 \pm 0.003$		$0.013 \pm 0.001$		$\mu_N^2$
	$B(E2; 2_2^+ \rightarrow 0_{g.s.}^+)$	$< 0.30$ [6]	$0.44 \pm 0.27$		$4.84 \pm 1.98$		$\text{e}^2\text{fm}^4$
	$\text{BR}(2_2^+ \rightarrow 2_1^+)$	$> 91.2$ [6]	$83 \pm 11^a$	$86 \pm 11^b$	$32 \pm 9^a$	$19 \pm 10^b$	%
	$\lambda_{\text{Total}}(2_2^+)$	[2.25, 4.10]	$3.2 \pm 0.7^a$	$4.9 \pm 1.5^b$	$8.6 \pm 2.4^a$	$20.6 \pm 8.6^b$	$10^{12}/\text{s}$
$4_1^+$	$\tau(2_2^+)$	[244, 446]	$316 \pm 66^a$	$204 \pm 64^b$	$116 \pm 32^a$	$49 \pm 20^b$	fs
	$E(4_1^+)$	$4129.0 \pm 0.2$	$4500 \pm 250$		$6170 \pm 100$		keV
	$B(E2; 4_1^+ \rightarrow 2_1^+)$	[2.74, 6.10]	$> 2.6$		$1.96 \pm 0.80$		$\text{e}^2\text{fm}^4$
	$\tau(4_1^+)$	[1.8, 4]	$< 4.22^a$	$< 1.68^b$	$5.59_{-1.62}^{+3.86^a}$	$0.57_{-0.16}^{+0.40^b}$	ps

<sup>a</sup>Using the experimental transition energy<sup>b</sup>Using the theoretical transition energy

showing strong sensitivity to the underlying nuclear interaction, and in particular to the inclusion of 3N forces. Our experiment has delivered key experimental data to constrain modern nuclear theories. Ab initio NCSM calculations employing new interactions derived within chiral EFT show remarkable agreement with experiment, a very promising step towards describing nuclear structure from first principles. They also show that  $E2$  transitions present a specific challenge for ab initio methods and require further methodological improvements to provide more accurate predictions for these important observables.

**Acknowledgements** This work was supported by the Deutsche Forschungsgemeinschaft (DFG, German Research Foundation)—Projektnummer 279384907—SFB 1245, the Royal Society under contract number UF150476, the UK STFC under grant numbers ST/L005727/1 and ST/P003885/1, the U.S. Department of Energy, Office of Science, Office of Nuclear Physics, under Contract Nos. DE-AC02-06CH11357 (ANL), DE-AC02-05CH11231 (LBNL) and DE-AC05-00OR22725 (ORNL), the U.S. NSF under grant No. PHY-2012522 and the National Research Foundation of South Africa (Grant No. 118846). This research used resources of ANL's ATLAS Facility, which is a DOE Office of Science User Facility. The authors thank J. T. Anderson and M. B. Oberling for technical support, J. P. Greene for the preparation of the target, and the ATLAS accelerator crew for their supreme effort.

**Data Availability Statement** Data will be made available on reasonable request. [Authors' comment: The datasets generated during and/or analysed during the current study are available from the corresponding author on reasonable request.]

**Code Availability Statement** Code/software will be made available on reasonable request. [Author's comment: The code/software generated

during and/or analysed during the current study is available from the corresponding author on reasonable requests.]

**Open Access** This article is licensed under a Creative Commons Attribution 4.0 International License, which permits use, sharing, adaptation, distribution and reproduction in any medium or format, as long as you give appropriate credit to the original author(s) and the source, provide a link to the Creative Commons licence, and indicate if changes were made. The images or other third party material in this article are included in the article's Creative Commons licence, unless indicated otherwise in a credit line to the material. If material is not included in the article's Creative Commons licence and your intended use is not permitted by statutory regulation or exceeds the permitted use, you will need to obtain permission directly from the copyright holder. To view a copy of this licence, visit <http://creativecommons.org/licenses/by/4.0/>.

## References

1. E. Epelbaum, H.W. Hammer, U.G. Meißner, Rev. Modern Phys. **81**(4), 1773 (2009). <https://doi.org/10.1103/revmodphys.81.1773>
2. E. Epelbaum, H. Krebs, D. Lee, U.G. Meißner, Phys. Rev. Lett. **106**, 192501 (2011). <https://doi.org/10.1103/PhysRevLett.106.192501>
3. P. Navrátil, J.P. Vary, B.R. Barrett, Phys. Rev. Lett. **84**, 5728 (2000). <https://doi.org/10.1103/PhysRevLett.84.5728>
4. P. Navrátil, S. Quaglioni, I. Stetcu, B.R. Barrett, **36**(8), 083101 (2009). doi: <https://doi.org/10.1088/0954-3899/36/8/083101>
5. C. Forssén, R. Roth, P. Navrátil, J. Phys. G Nucl. Part. Phys. **40**(5), 055105 (2013). <https://doi.org/10.1088/0954-3899/40/5/055105>
6. M. Petri, S. Paschalis, R.M. Clark, P. Fallon, A.O. Macchiavelli, K. Starosta, T. Baugher, D. Bazin, L. Cartegni, H.L. Crawford, M. Cromaz, U. Datta Pramanik, G. de Angelis, A. Dewald, A. Gade, G.F. Grinyer, S. Gros, M. Hackstein, H.B. Jeppesen, I.Y. Lee, S. McDaniel, D. Miller, M.M. Rajabali, A. Ratkiewicz, W. Rother, P. Voss, K.A. Walsh, D. Weisshaar, M. Wiedeking, B.A. Brown,

- C. Forssén, P. Navrátil, R. Roth, *Phys. Rev. C* **86**, 044329 (2012). <https://doi.org/10.1103/PhysRevC.86.044329>
7. M. Ciemala, S. Ziliani, F.C.L. Crespi, S. Leoni, B. Fornal, A. Maj, P. Bednarczyk, G. Benzoni, A. Bracco, C. Boiano, S. Bottoni, S. Brambilla, M. Bast, M. Beckers, T. Braunroth, F. Camera, N. Cieplicka-Oryńczak, E. Clément, S. Coelli, O. Dorvaux, S. Erturk, G. de France, C. Fransén, A. Goldkuhle, J. Grębosz, M.N. Harakeh, L.W. Iskra, B. Jacquot, A. Karpov, M. Habior, Y. Kim, M. Kmiecik, A. Lemasson, S.M. Lenzi, M. Lewitowicz, H. Li, I. Matea, K. Mazurek, C. Michelagnoli, M. Matejska-Minda, B. Million, C. Müller-Gatermann, V. Nanal, P. Napiorkowski, D.R. Napoli, R. Palit, M. Rejmund, C. Schmitt, M. Stanoiu, I. Stefan, E. Vardaci, B. Wasilewska, O. Wieland, M. Zieblinski, M. Zielińska, A. Atač, D. Barrientos, B. Birkenbach, A.J. Boston, B. Cederwall, L. Charles, J. Collado, D.M. Cullen, P. Désesquelles, C. Domingo-Pardo, J. Dudouet, J. Eberth, V. González, J. Goupil, L.J. Harkness-Brennan, H. Hess, D.S. Judson, A. Jungclaus, W. Kortén, M. Labiche, A. Lefevre, R. Menegazzo, D. Mengoni, J. Nyberg, R.M. Perez-Vidal, Z. Podolyak, A. Pullia, F. Recchia, P. Reiter, F. Saillant, M.D. Salsac, E. Sanchis, O. Stezowski, C. Theisen, J.J. Valiente-Dobón, J.D. Holt, J. Menéndez, A. Schwenk, J. Simonis, *Phys. Rev. C* **101**, 021303 (2020). <https://doi.org/10.1103/PhysRevC.101.021303>
  8. M. Wiedeking, P. Fallon, A.O. Macchiavelli, J. Gibelin, M.S. Basunia, R.M. Clark, M. Cromaz, M.A. Deleplanque, S. Gros, H.B. Jeppesen, P.T. Lake, I.Y. Lee, L.G. Moretto, J. Pavan, L. Phair, E. Rodriguez-Vietez, L.A. Bernstein, D.L. Bleuel, J.T. Burke, S.R. Leshner, B.F. Lyles, N.D. Scielzo, *Phys. Rev. Lett.* **100**, 152501 (2008). <https://doi.org/10.1103/PhysRevLett.100.152501>
  9. H.J. Ong, N. Imai, D. Suzuki, H. Iwasaki, H. Sakurai, T.K. Onishi, M.K. Suzuki, S. Ota, S. Takeuchi, T. Nakao, Y. Togano, Y. Kondo, N. Aoi, H. Baba, S. Bishop, Y. Ichikawa, M. Ishihara, T. Kubo, K. Kurita, T. Motobayashi, T. Nakamura, T. Okumura, Y. Yanagisawa, *Phys. Rev. C* **78**, 014308 (2008). <https://doi.org/10.1103/PhysRevC.78.014308>
  10. I.Y. Lee, *Nucl. Phys. A* **520**, c641 (1990). [https://doi.org/10.1016/0375-9474\(90\)91181-P](https://doi.org/10.1016/0375-9474(90)91181-P)
  11. D. Sarantites, P.F. Hua, M. Devlin, L. Sobotka, J. Elson, J. Hood, D. LaFosse, J. Sarantites, M. Maier, *Nucl. Instr. Meth. Phys. Res. A* **381**(2), 418 (1996). [https://doi.org/10.1016/S0168-9002\(96\)00785-1](https://doi.org/10.1016/S0168-9002(96)00785-1)
  12. M. Mathy, *Electromagnetic Properties of Light Neutron-Rich Nuclei - Lifetime Measurements of  $^{16}\text{C}$  and  $^{23}\text{Ne}$* . Ph.D. thesis, Technische Universität Darmstadt (2020)
  13. M.A. Eswaran, C. Broude, *Can. J. Phys.* **42**, 1311 (1964)
  14. E.K. Warburton, J.W. Olness, A.R. Poletti, *Phys. Rev.* **160**, 938 (1967). <https://doi.org/10.1103/PhysRev.160.938>
  15. W. Kutschera, D. Pelte, G. Schrieder, *Nucl. Phys. A* **111**(3), 529 (1968). [https://doi.org/10.1016/0375-9474\(68\)90237-6](https://doi.org/10.1016/0375-9474(68)90237-6)
  16. C. Broude, P. Engelstein, M. Popp, P. Tandon, *Phys. Lett. B* **39**(2), 185 (1972). [https://doi.org/10.1016/0370-2693\(72\)90769-1](https://doi.org/10.1016/0370-2693(72)90769-1)
  17. L.K. Fifield, R.W. Zurmühle, D.P. Balamuth, *Phys. Rev. C* **10**, 1785 (1974). <https://doi.org/10.1103/PhysRevC.10.1785>
  18. L. Ekström, D. Scherpenzeel, G. Engelbertink, H. Aarts, H. Eggenhuisen, *Nucl. Phys. A* **295**(3), 525 (1978). [https://doi.org/10.1016/0375-9474\(78\)90190-2](https://doi.org/10.1016/0375-9474(78)90190-2)
  19. L.K. Fifield, J. Asher, A.R. Poletti, *J. Phys. G Nucl. Part. Phys.* **4**(3), L65 (1978). <https://doi.org/10.1088/0305-4616/4/3/005>
  20. J. Forster, T. Alexander, G. Ball, W. Davies, I. Mitchell, K. Winterbon, *Nucl. Phys. A* **313**(3), 397 (1979). [https://doi.org/10.1016/0375-9474\(79\)90509-8](https://doi.org/10.1016/0375-9474(79)90509-8)
  21. M. Shamsuzzoha Basunia. *Nucl. Data Sheets* 127, 69(2015). <https://www.nndc.bnl.gov/nudat2/getdataset.jsp?nucleus=22NE&unc=nds> (2015). [Online; accessed 31th July 2020]
  22. ICRU, *Journal of the International Commission on Radiation Units and Measurements* **5**(1), iii (2005). doi: 10.1093/jicru/ndi002
  23. S. Heil, *Simulation of gamma-ray detector arrays for nuclear physics experiments*. Master's thesis, Technische Universität Darmstadt (2015)
  24. J.F. Ziegler, M. Ziegler, J. Biersack, *Nucl. Instr. Meth. Phys. Res. B* **268**(11), 1818 (2010). doi: <https://doi.org/10.1016/j.nimb.2010.02.091>. <http://www.sciencedirect.com/science/article/pii/S0168583X10001862>. 19th International Conference on Ion Beam Analysis
  25. G.J. Feldman, R.D. Cousins, *Phys. Rev. D* **57**, 3873 (1998). <https://doi.org/10.1103/PhysRevD.57.3873>
  26. K. Tsukiyama, S.K. Bogner, A. Schwenk, *Phys. Rev. C* **85**, 061304 (2012). <https://doi.org/10.1103/PhysRevC.85.061304>
  27. S.R. Stroberg, A. Calci, H. Hergert, J.D. Holt, S.K. Bogner, R. Roth, A. Schwenk, *Phys. Rev. Lett.* **118**(3), 032502 (2017). <https://doi.org/10.1103/PhysRevLett.118.032502>
  28. E. Gebrerufael, K. Vobig, H. Hergert, R. Roth, *Phys. Rev. Lett.* **118**(15), 152503 (2017). <https://doi.org/10.1103/PhysRevLett.118.152503>
  29. S.R. Stroberg, J. Henderson, G. Hackman, P. Ruotsalainen, G. Hagen, J.D. Holt, *Phys. Rev. C* **105**(3), 034333 (2022). <https://doi.org/10.1103/PhysRevC.105.034333>
  30. A. Tichai, J. Müller, K. Vobig, R. Roth, *Phys. Rev. C* **99**(3), 034321 (2019). <https://doi.org/10.1103/PhysRevC.99.034321>
  31. T. Hüther, K. Vobig, K. Hebel, R. Machleidt, R. Roth, *Phys. Lett. B* **808**, 135651 (2020). <https://doi.org/10.1016/j.physletb.2020.135651>
  32. R. Roth, J. Langhammer, A. Calci, S. Binder, P. Navrátil, *Phys. Rev. Lett.* **107**, 072501 (2011). <https://doi.org/10.1103/PhysRevLett.107.072501>
  33. R. Roth, A. Calci, J. Langhammer, S. Binder, *Phys. Rev. C* **90**(2), 024325 (2014). <https://doi.org/10.1103/PhysRevC.90.024325>
  34. H.J. Ong, N. Imai, D. Suzuki, H. Iwasaki, H. Sakurai, T.K. Onishi, M.K. Suzuki, S. Ota, S. Takeuchi, T. Nakao, Y. Togano, Y. Kondo, N. Aoi, H. Baba, S. Bishop, Y. Ichikawa, M. Ishihara, T. Kubo, K. Kurita, T. Motobayashi, T. Nakamura, T. Okumura, Y. Yanagisawa, *Phys. Rev. C* **78**, 014308 (2008). <https://doi.org/10.1103/PhysRevC.78.014308>